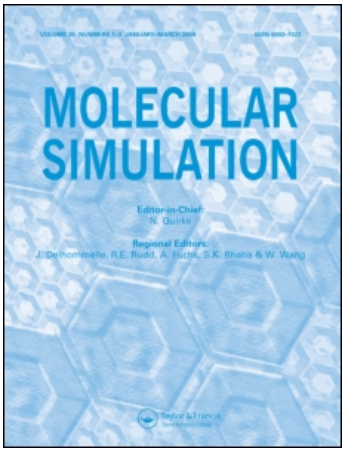

Molecular Simulation
Publication details, including instructions for authors and subscription information:
http://www.informaworld.com/smpp/title~content=t713644482

Phase behaviour and separation kinetics of symmetric non-additive hard discs

Laura Muñoz-Salazar[a]; Gerardo Odriozola[b]
[a] Programa de Posgrado, Instituto Mexicano del Petróleo, México, D.F, México [b] Programa de Ingeniería Molecular, Instituto Mexicano del Petróleo, México, D.F, México

First published on: 27 August 2009

To cite this Article Muñoz-Salazar, Laura and Odriozola, Gerardo(2010) 'Phase behaviour and separation kinetics of symmetric non-additive hard discs', Molecular Simulation, 36: 3, 175 — 185, First published on: 27 August 2009 (iFirst)
To link to this Article: DOI: 10.1080/08927020903141027
URL: http://dx.doi.org/10.1080/08927020903141027

Molecular Simulation
Vol. 36, No. 3, March 2010, 175–185

Taylor & Francis
Taylor & Francis Group

Phase behaviour and separation kinetics of symmetric non-additive hard discs

Laura Muñoz-Salazar[a] and Gerardo Odriozola[b]*

[a]*Programa de Posgrado, Instituto Mexicano del Petróleo, Lázaro Cárdenas 152, 07730 México, D.F., México;* [b]*Programa de Ingeniería Molecular, Instituto Mexicano del Petróleo, Lázaro Cárdenas 152, 07730 México, D.F., México*

(*Received 30 January 2009; final version received 24 June 2009*)

The phase separation of symmetric non-additive hard discs mixtures is studied. For that purpose, Monte Carlo simulations are implemented for accessing both phase separation behaviour and its kinetics. The latter is monitored by the evolution of the cluster size distribution of the less concentrated species. The kinetic data are then compared to the stochastic solutions of the master equation, which constitute a reduced description of the same phenomenon. The obtained good agreement points out the success of this simple numerical method for correctly describing the reversible nature of the drop-like clusters.

Keywords: kinetics; liquid phase separation; non-additivity

1. Introduction

It is common use in physics to average out relatively small and fast moving particles from the system to gain simplicity on the framework to be developed, i.e. to integrate out a subset of degrees of freedom [1–3]. A few examples are: expressing the Hamiltonian of a system as a function of the nuclear variables only, by averaging out the rapid motion of electrons; integrating out positions and momenta of the solvent to obtain the effective interactions between larger colloidal particles; and even considering fluids as continuous medium when dealing with engineer-scale problems of mass, heat and momentum transfer [4]. In the same spirit, in this work, we attempt to obtain a dynamic and structural reduced description of a binary mixture by only explicitly taking into account the aggregation state – the cluster size distribution (CSD) – of the less concentrated species.

In order to build this CSD-based description, it is necessary to first obtain the correct behaviour of the binary mixture by means of well-established computational techniques. Thus, different types of Monte Carlo (MC) simulations are performed to gain insight into the many dynamical and structural aspects of this system. For the sake of simplicity, the studied system is a two-dimensional (2D) mixture of positive and symmetrical non-additive hard discs (NAHD). We choose the NAHD mixture since, to our knowledge, this is one of the simplest binary models which shows phase separation at certain conditions [5,6]. In addition, 2D non-additive interactions have been used to study the morphology of composite polymer particles [7], and the solubility of molecular additives in different solvents [8]. Finally, this model has no energetic contribution to the system free energy, and so phase separation is purely entropy-driven (many phase separation processes in the colloidal domain are ruled by entropy [9]).

Once the phase behaviour and the kinetic description are obtained, for different conditions and by means of simulations, one is ready to implement the master equation approach to the same phenomena. This formalism describes the time evolution of the probability of the system to occupy each one of a discrete set of states, and has been successfully applied to many different physical phenomena ranging from quantum field theory to colloidal aggregation, passing through chemical reactions [10–14]. In our case, the states are defined by the CSD of the less concentrated species only, and consequently, the amount of information to be handled is strongly reduced (all particle positions and momenta are not explicitly considered).

The paper is structured as follows: Section 1 is this brief introduction. Section 2 details the numerical methods employed in this work: simulations and the master equation approach. In Section 3, we show the obtained results. Finally, Section 4 highlights the most important contributions.

2. Numerical techniques

2.1 Simulations

The NAHD model [5,6] is employed for studying the phase separation of a binary fluid. This model consists of a mixture of hard discs A and B of diameter $\sigma_A = \sigma_B = \sigma$ (we forced symmetry between A and B particles), which

*Corresponding author. Email: godriozo@imp.mx

ISSN 0892-7022 print/ISSN 1029-0435 online

DOI: 10.1080/08927020903141027
http://www.informaworld.com

interact by means of

$$U_{ii}(r) = \begin{cases} \infty & \text{for } r \leq \sigma, \\ 0 & \text{for } r > \sigma, \end{cases}$$

$$U_{ij}(r) = \begin{cases} \infty & \text{for } r \leq \sigma(1+\Delta), \\ 0 & \text{for } r > \sigma(1+\Delta), \end{cases}$$

where U_{ii} (i = A or B) is the pair potential energy for like particles, U_{ij} (j = A or B and $j \neq i$) is the pair potential energy for unlike particles, r is the distance between the centres of the interacting particles and Δ is the non-additive parameter.

For a negative value of the non-additivity parameter ($\Delta < 0$), the binary mixture shows a tendency to form A–B coordinated clusters, i.e. to form a mixture of A–B particles. On the other hand, for a positive non-additivity ($\Delta > 0$), the system tends to segregate A and B particles. That is, to increase entropy (to gain free accessible space), the binary mixture decreases the number of A–B pairs. When the total system density reaches a large enough value, the mixture phase separates yielding A-rich and B-rich phases. For a relatively small A particle concentration, the overall behaviour can be seen as the growing of A clusters. We focus our attention on this process, setting $\Delta = 0.2$ and working with A diluted systems.

The system is defined on a square 2D cell with side $L = 80\sigma$ (unless otherwise indicated). Initially, N_A A-particles and N_B B-particles are randomly placed inside the cell avoiding overlaps. Then, three different simulation techniques are used to make the system evolve. Semigrand canonical ensemble MC simulations are used to produce the coexistence curve for a given total number of particles, $N_T = N_A + N_B$ [15,16]. This technique uses the standard MC particle displacements, together with identity exchange and interchange trials. Identity exchange trials consist of choosing a particle and trying to switch its type from A to B or vice versa. Interchange trials are done by choosing two particles of different types and attempting to interchange their labels (A → B and B → A). Thus, identity exchanges lead to fluctuations of N_A and N_B keeping a constant N_T, while interchange changes also keep N_A and N_B unchanged. These trials yield, for small Δ, a fast evolution of the system towards equilibrium, given a total number density $\rho_T = N_T\sigma^2/L^2$. For large Δ values, cluster moves are shown to be more efficient [17]. This type of simulation allows us to measure the relative A-particle fraction, $X_A = N_A/N_T$. For conditions around the consolute point, (X_A^c, ρ_T^c), fluctuations make it difficult to determine the coexistence curve. Consequently, it is useful to measure (X_A^c, ρ_T^c). This is done by monitoring the reduced second moment of $m \equiv 2X_A - 1$, $\text{rsm} = \langle m^2\rangle/\langle|m|\rangle^2$, as described elsewhere [18–20]. This method relies on the fact that the rsm is independent of the system size at the consolute point. Another possible way of determining (X_A^c, ρ_T^c) is given elsewhere [17].

The coexistence curve guides us to set the conditions (X_A, ρ_T) for studying different equilibrium states and separation kinetics. The study of the equilibrium states is achieved by a MC technique (second type of MC), where particle displacements and interchange trials are performed. Additionally, the cluster growth is tackled by means of a MC technique where only small particle displacements are tried (third type of MC). This leads to an approximated direct relationship between the number of simulation steps and time [21,22] (this can be safely done for hard core interactions [22]), and so, kinetic information can be accessed. This information is measured as the evolution of the CSD of the less concentrated species with the number of steps. For that purpose, a cluster is defined as a collection of bonded A-particles; and a bond is formed by those A-pairs having a centre to centre distance smaller than a bonding radius, $r_b = 1.5\sigma$. Let us refer to this MC technique as Brownian dynamics (BD) simulations.

2.2 *Kinetic background*

In the classic aggregation framework, the time evolution of the CSD of a diluted species, $\vec{N}(t) = (N_1, N_2, \ldots, N_i, \ldots)$, N_i being the number of i-size clusters of A-particles, is described by the well-known Smoluchowski's equation [23,24]. This equation can be rewritten in terms of a master equation to capture both aggregation and fragmentation events [11,12,25]. It reads

$$\begin{aligned} \frac{dP(\vec{N},t)}{dt} = \frac{1}{2L^2}\sum_{i,j} k_{ij}\Big[&(N_i+1)\big(N_j+1+\partial_{ij}\big)P\Big(\vec{N}_{ij}^{+},t\Big) \\ &-N_i\big(N_j-\partial_{ij}\big)P\Big(\vec{N},t\Big)\Big] \\ &+\frac{1}{2}\sum_{n=2}\Bigg[(N_n+1)\sum_{i=1}^{n-1} f_{i(n-i)}P\Big(\vec{N}_{i(n-i)}^{-},t\Big) \\ &-N_n\sum_{i=1}^{n-1} f_{i(n-i)}P\Big(\vec{N},t\Big)\Bigg], \end{aligned} \tag{1}$$

where the states $\vec{N}_{ij}^{+}$ and $\vec{N}_{ij}^{-}$ are given by

$$\vec{N}_{ij}^{+} = \begin{cases} (\ldots, N_i+1, \ldots, N_j+1, \ldots, N_{i+j}-1, \ldots) & \text{for } i \neq j, \\ (\ldots, N_i+2, \ldots, N_{2i}-1, \ldots) & \text{for } i = j, \end{cases}$$

$$\vec{N}_{ij}^{-} = \begin{cases} (\ldots, N_i-1, \ldots, N_j-1, \ldots, N_{i+j}+1, \ldots) & \text{for } i \neq j, \\ (\ldots, N_i-2, \ldots, N_{2i}+1, \ldots) & \text{for } i = j. \end{cases}$$

Here, $P(\vec{N},t)$ represents the system probability of finding the system at the state $\vec{N}$ at time t, k_{ij} is the

aggregation kernel, f_{ij} is the fragmentation kernel, L^2 is the area of the system cell, and δ_{ij} is the Kronecker delta function. k_{ij} represents the ij element of the matrix of rate constants for which an i-size cluster joins to a j-size cluster. On the other hand, f_{ij} is the ij element of the matrix of rate constants for which an $(i+j)$-size cluster separates into child i and j clusters. Both kernels must be understood as orientational and configurational averages, which contain the relevant physical information.

When all cluster encounters lead to a larger cluster formation and no breakup events exist, the time evolution of $\vec{N}$ is obtained by solving Equation (1) with $f_{ij} = 0$ and

$$k_{ij} = \frac{1}{2} k_{11} \left(i^{-1/d_f} + j^{-1/d_f} \right), \tag{2}$$

where k_{ij} stands for the 2D Brownian kernel [26–28], d_f is the cluster fractal dimension and k_{11} is the dimer formation rate constant. These conditions yield the well-known diffusion-limited cluster aggregation regime (DLCA) [29,30].

For reversible processes, the following fragmentation kernel has been proposed [25]:

$$f_{ij} = e_{ij}\left(1 + \delta_{ij}\right)/(\tau \mathcal{N}_{ij}), \tag{3}$$

where τ is the average dimer bond lifetime, the e_{ij} element gives the number of bonds contained in an n-size cluster, which, on breakup, lead to i and j size fragments, and $\mathcal{N}_{ij}$ is the average number of consecutive collisions that two recently formed and space-correlated child clusters perform before diffusing away. This ij entry is given by $\mathcal{N}_{ij} = \mathcal{N}_{11}(ij)^b$, $\mathcal{N}_{11}$ and b being parameters to be determined [31–33].

Expressions (1)–(3) model a system where all collisions lead to bond formation and the produced bonds live an average time τ [25]. Briefly, it models an effective A–A pair potential having no barrier and an energetic well close to the A–A contact.

3. Results

3.1 Phase diagram

As mentioned in Section 2.1, the NAHD model phase separates for $\Delta > 0$ and a sufficiently large total number density, ρ_T. The coexistence curve, determined by means of the semigrand canonical technique, is given in Figure 1 for $L = 50\sigma$, 80σ and 100σ. As can be seen, both conditions produce the same curve, which agree with the data shown by Figure 2 of reference [6]. Note that the coexistence curve is symmetric with respect to X_A (or $X_B = 1 - X_A$), since we forced A and B particles to have the same diameter. The consolute point, i.e. the total number density for $X_A = 0.5$, corresponds to the value given by the intersection of the curves shown in Figure 2.

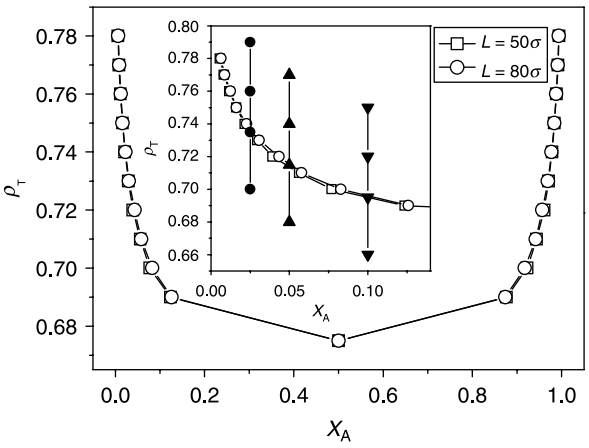

Figure 1. Coexistence curve for $\Delta = 0.2$. Open square symbols are obtained for $L = 50\sigma$ and open circles are for $L = 80\sigma$. The inset zooms in the same data. Additionally, solid symbols point out the conditions for which kinetic data are obtained.

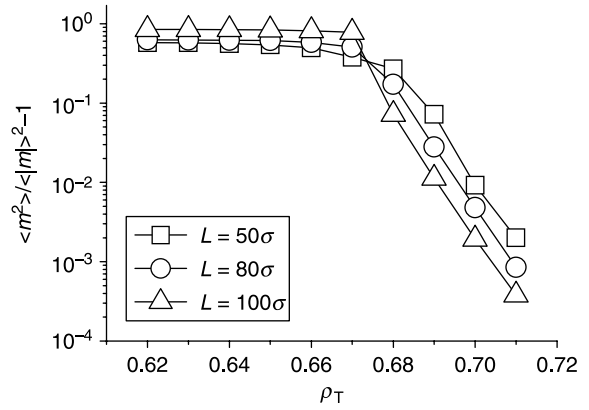

Figure 2. $\langle m^2\rangle/\langle|m|\rangle^2 - 1$ is plotted as a function of the total density, ρ_T, for $L = 50\sigma$ (□), 80σ (○) and 100σ (△). The obtained consolute total density is $\rho_T^c \approx 0.675$, given by the point at which the curves cross.

We obtain a consolute number density value of $\rho_T^c \approx 0.675$.

In Figure 2, the fluctuations of X_A, quantified by rsm, become smaller by increasing the cell size when the system is phase separated ($\rho_T > \rho_T^c$). On the contrary, by increasing the cell size, the fluctuations become larger for mixed systems ($\rho_T < \rho_T^c$). Thus, the decrease in the fluctuations with ρ_T is sharper for larger systems. As already mentioned, the system size has no effect on the fluctuations for the consolute number density.

Since the stochastic approach to be implemented for describing the kinetics is reliable only for small concentrations of the aggregating species, A-particles, we focus our attention on $X_A \leq 0.1$. Specifically, as shown in the inset of Figure 1, we set runs for $X_A = 0.025$, 0.050 and 0.100. Having these conditions fixed, ρ_T is set in order

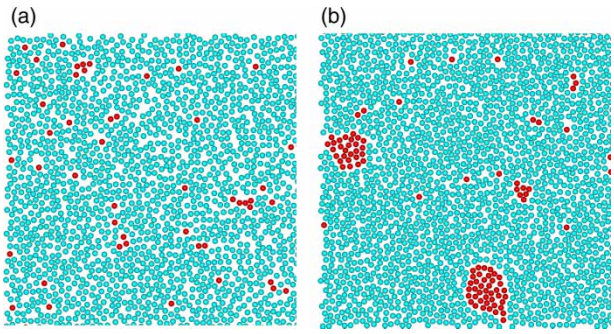

Figure 3. Snapshots (a quarter of the simulation cell) of equilibrium configurations for $L = 80\sigma$ and $X_A = 0.025$. (a) For $\rho = 0.70$ and (b) for $\rho = 0.79$. A-particles are dark red and B-particles are sky blue.

Table 1. Conditions at which kinetic data are collected[a].

X_A	ρ_T			
0.025	0.700 (a)	0.735 (b)	0.760 (c)	0.790 (d)
0.050	0.680 (e)	0.715 (f)	0.740 (g)	0.770 (h)
0.100	0.660 (i)	0.695 (j)	0.720 (k)	0.750 (l)

[a] They correspond to the solid symbols shown in the inset of Figure 1.

to study the equilibrium and aggregation kinetics on the coexistence curve, over and under it, as shown by the solid symbols of the inset of Figure 1. The corresponding number values are given in Table 1.

As explained, equilibrium is achieved by a MC technique using displacement and interchange trials. A snapshot of an equilibrium configuration for $X_A = 0.025$ and $\rho = 0.70$, i.e. under the coexistence curve, is shown in Figure 3(a). As can be seen, clusters grow producing only few oligomers. Accordingly, phase separation does not occur. On the other hand, Figure 3(b) shows an equilibrium configuration for $X_A = 0.025$ and $\rho = 0.79$, which is well over the coexistence curve. In this case, A-clusters grow yielding large sizes and consuming almost all monomers.

3.2 *Cluster growth kinetics*

In Section 2.1, we stated that cluster growth kinetics can be accessed by performing MC simulations where only short displacements are tried, since there exists an approximately linear relationship between the performed number of steps and time (BD simulations [21,22]). For instance, assuming the particles to be immersed in water at 298 K, and for $\sigma = 100$ nm, a relationship is obtained between steps and time of approximately 1.37×10^{-5} s step^{-1} for all ρ_T. This relationship arises from the comparison of the diffusion coefficients as obtained by MC and smart MC (smart MC is shown to produce BD results elsewhere [22]; BD cannot be implemented for hard core interactions).

The evolution of the normalised CSD with the number of steps obtained by BD for $X_A = 0.025$ and $\rho_T = 0.70$ is given in Figure 4(a), as well as the corresponding equilibrium CSD (solid symbols). The CSD is normalised by the initial number of monomers, which coincides with the number of A-particles, N_A. It is observed that the number of monomeric units decreases to form oligomers. This occurs during the first 10^6 steps yielding at most 8–12-mers. From this point on, the system reaches equilibrium and the number of the different n-mers fluctuates around average values. These average values coincide with the data obtained by equilibrium MC simulations [solid symbols of Figure 4(a)], where interchange trials are performed and a large number of configurations are averaged.

Figure 4(b) shows the data obtained for $X_A = 0.025$ and $\rho_T = 0.79$. In this case, it seems that equilibrium is not

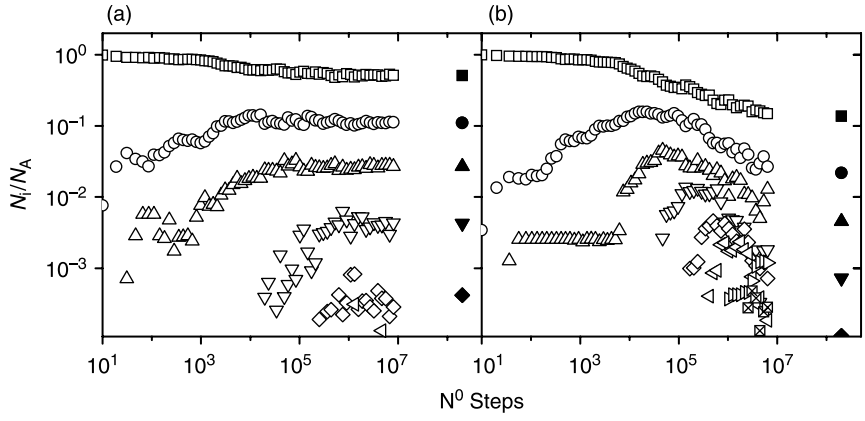

Figure 4. Evolution of the normalized CSD for $X_A = 0.025$ and $\rho_T = 0.70$ (a) and $\rho_T = 0.79$ (b). The symbols correspond to monomers up to 50-mers grouped in logarithmically spaced intervals: (□) monomers, (○) dimers, (△) 3–4-mers, (▽) 5–7-mers, (◇) 8–12-mers, (◁) 13–20-mers, (▷) 21–32-mers, and (⊠) 33–50-mers. Solid symbols correspond to equilibrium.

reached by the approximately 10^7 steps performed by the BD simulations. This statement is supported by the fact that the data obtained by the equilibrium MC simulations [solid symbols of Figure 4(b)] do not completely coincide with the final steps of the kinetic data. On the other hand, it is also observed that the decay of the relative number of monomers is approximately four times larger than for the previous case. Additionally, few large clusters which concentrate most of the A-particles are found by the equilibrium MC technique [see Figure 3(b)]. That is, the system phase separates.

The phase separation can also be pointed out by the weight average cluster size, $n_w = \sum_i i^2 N_i / \sum_i i N_i$. This quantity equals one for monodisperse conditions and rises with increasing cluster size. Its evolution is given in Figure 5 for all runs. n_w reaches higher values for larger X_A, since a larger A concentration leads to bigger clusters [compare the y-axes of Figure 5(a)–(c)]. For a given X_A, the short time behaviour of n_w is quite independent of the total concentration, ρ_T, whereas it strongly differs at long times. The almost independent short time behaviour is due to the fact that the increase of ρ_T leads to a larger ρ_A and a larger bond lifetime (see Section 3.5), which is compensated by a decrease of the monomer diffusion coefficient (see Section 3.3). On the other hand, the larger bond lifetime makes n_w increase at long times for large ρ_T, producing a higher equilibrium n_w value. In fact, the equilibrium n_w values show a sharper increase (close to an order of magnitude larger) with ρ_T for those conditions which lead to phase separation (each graph in Figure 5 includes a dotted line among the data showing phase separation and the data not showing phase separation). Finally, it should be noted that equilibrium is reached for the systems that do not phase separate (solid symbols equal the averages of the n_w long time values), whereas n_w for systems having phase separation does not yield the equilibrium values.

Up to here, the phase separation kinetics have been described in terms of the BD simulations. From here on, we will focus our attention on generating the stochastic solutions of Equation (1), by using (2) and (3). For that purpose, we are forced to gain further insight into the phenomenon to obtain the dimer formation rate constant, k_{11}, the cluster fractal dimension, d_f, the average dimer bond lifetime, τ, and elements e_{ij}.

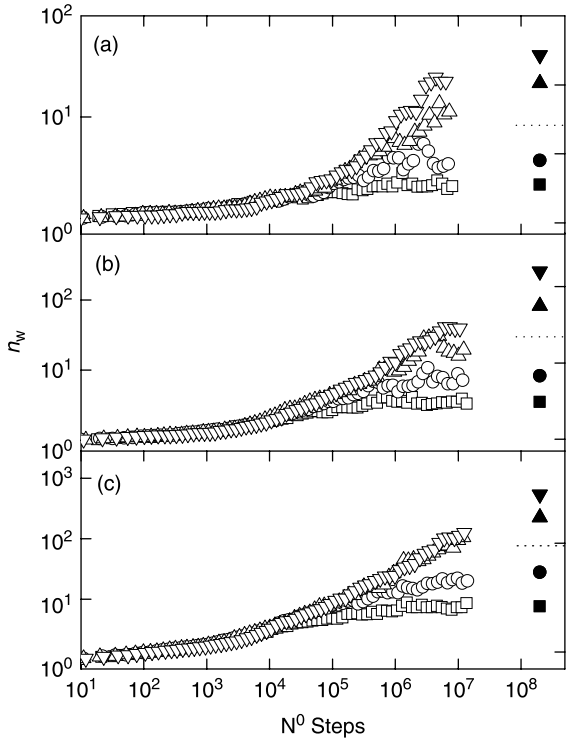

Figure 5. Evolution of the weight average cluster size, n_w, for all conditions: (a) $X_A = 0.025$, (b) $X_A = 0.050$, and (c) $X_A = 0.100$. Symbols □, ○, △ and ▽ correspond to the lowest, low-intermediate, high-intermediate and highest total densities, ρ_T, respectively, as plotted in the inset of Figure 1 and given in Table 1. Solid symbols are obtained at equilibrium. Dotted lines separate the runs with (X_A,ρ_T) points above the coexistence curve from those with (X_A,ρ_T) points under it.

3.3 Monomer diffusion

The dimer formation rate constant, k_{11}, assumed to be equal to the collision frequency, is directly proportional to the monomer (A-particle) diffusion coefficient, D_1. Hence, $k_{11} = CD_1$, where C is a constant which should not depend on X_A or ρ_T. On the other hand, the diffusion coefficient can be measured from simulations by means of the 2D Einstein relationship

$$D_1 = \lim_{t\to\infty} \frac{\langle r(t)^2 \rangle}{4t}, \tag{4}$$

where $\langle r(t)^2 \rangle$ is the mean square displacement and t is the elapsed time (in our case, the number of steps of the BD simulation). So, D_1 can be obtained from a simulation where A-particles are dilute enough to guarantee no correlations among them.

The obtained D_1 values are given in Figure 6 as a function of the modified total number density $\rho_T f$, with

$$f = X_A^2 + (1 - X_A)^2 + 2X_A(1 - X_A)(1 + \Delta)^2. \tag{5}$$

Factor f introduces a correction of the total particle concentration to take into account the larger space occupied by the A–B pairs. It considers the A–B mixture as homogeneously distributed in space. As can be seen in Figure 6, for the considered range of $\rho_T f$, we obtain a linear decreasing behaviour of D_1. The fitting reads $D_1 = 0.00268 - 0.00306\rho_T f$. For larger $\rho_T f$ values, D_1 would exhibit a decreasing but nonlinear behaviour [34].

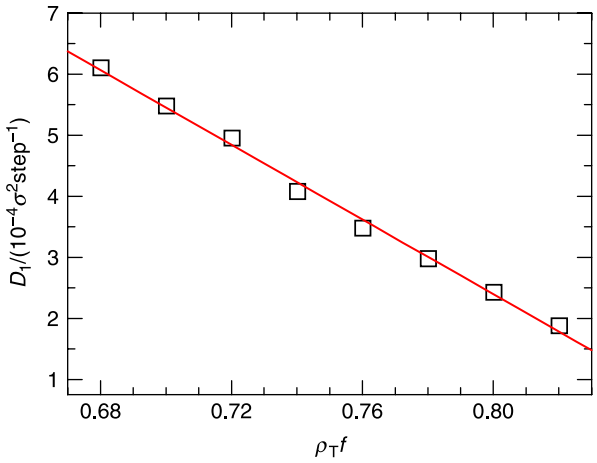

Figure 6. Diffusion coefficient of A-particles immersed in a bath of B-particles. A-particles are so dilute to guarantee no correlations among them.

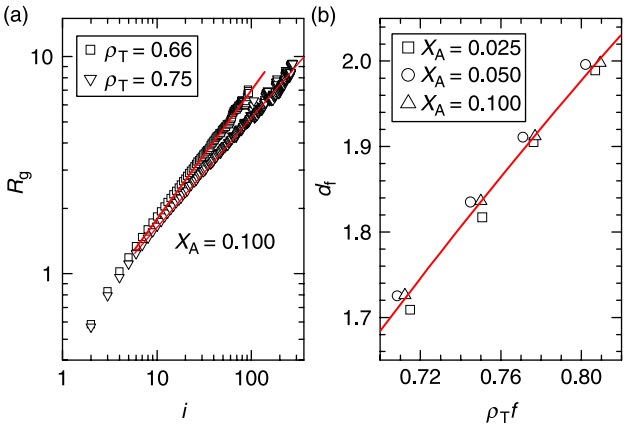

Figure 7. (a) Log–log graph of the clusters' gyration radii versus the cluster size for two systems with $X_A = 0.100$ and the total densities pointed out in the plot. (b) Fractal dimension as a function of the modified total density for all runs.

Thus, an extrapolation of the fit for larger $\rho_T f$ values surely leads to error.

As explained in Section 3.2, these results were compared to others obtained by means of smart MC (not shown) [22]. The smart MC results produce $D/D_0 = 0.8174 - 0.9330\rho_T f$ for the $\rho_T f$ range of [0.68,0.82], when considering water at room temperature as medium, $\sigma = 100\,\text{nm}$, and no hydrodynamic interactions. The comparison of both fits leads to a relationship of approximately $1.37 \times 10^{-5}\,\text{s step}^{-1}$ between steps and time, for $\rho_T f$ ranging in [0.68,0.82] and $D_0 = 2.4 \times 10^{-12}\,\text{m}^2\,\text{s}^{-1}$.

3.4 *Fractal dimension*

The cluster fractal dimension is a measurement of how the clusters fill the space. It affects the cluster diffusion which in turn controls the collision frequency. A larger fractal dimension implies a larger cluster diffusivity and a higher big-cluster big-cluster collision frequency. It is given by the relationship $R_g \sim i^{1/d_f}$, $R_g = \sqrt{1/i\sum_{j=1}^{i}|r_j - r_{cm}|^2}$ being the gyration radius of the clusters, i the cluster size, and $|r_j - r_{cm}|$ the distance between the monomer j of the given cluster and the cluster centre of mass. Since our cell is 2D, the fractal dimension, d_f, cannot surpass the limiting value of 2. For 2D rigid DLCA clusters, its reported value is 1.45 and for reaction limited cluster aggregation is 1.55 [26,28,35]. In our case, the structure of the clusters evolves with time since they are not only flexible but liquid-like. Nevertheless, we used the same framework to obtain average values of different clusters on different times (for rigid clusters the reported values are averages of different clusters only).

Figure 7(a) shows a log–log representation of R_g against the cluster size for systems having $X_A = 0.100$ and $\rho_T = 0.66$ and 0.75. In both cases a well-defined linear growth is obtained, from which average fractal dimensions can be accessed. These are 1.71 and 1.97, respectively, which are clearly above the values obtained by irreversible aggregation. These values point out the drop-like structure of the generated clusters. In addition, they reveal that larger total densities lead to much more compact clusters, as expected. In fact, the value 1.97 indicates that clusters are almost as compact as possible.

The fractal dimensions for all runs are plotted as a function of the modified total number density, $\rho_T f$, in Figure 7(b). As shown, d_f strongly increases with $\rho_T f$ for all X_A. Indeed, all data seem to define a master curve suggesting that d_f depends on X_A only trough factor f. The fit leads to $d_f = 1.381 + 5.648(\rho_T f) - 1.812(\rho_T f)^2$. As for the case of the diffusion coefficient, the fit cannot be extrapolated for large values of $\rho_T f$ (as mentioned, it cannot exceed the value of 2).

3.5 *Dimer bond lifetime*

In order to evaluate the fragmentation kernel, Expression (3), it is necessary to know the average dimer bond lifetime, τ. This quantity can be accessed by performing simulations of a system containing a dimer (two A-particles in contact) surrounded by a sea of B-particles. Setting the same maximum particle displacement as for the BD simulations, the number of steps needed to break the dimer (produce a particle–particle distance larger than the given bonding radius, $r_b = 1.5\sigma$) is registered. A histogram is built by repeatedly performing this procedure for different initial configurations of the B-particles at a given $\rho_T f$. Similar histograms are built for different values of $\rho_T f$. These histograms, once normalised, turn into the probability density functions (pdf) given in Figure 8(a). The inset of this figure shows the same data in

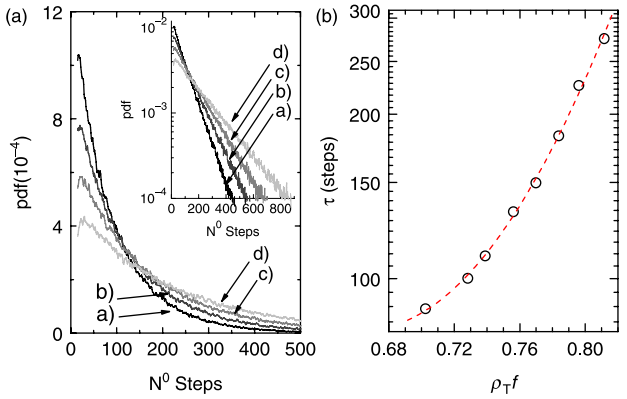

Figure 8. (a) Probability density for a breakup event of a dimer as a function of the number of steps. Labels (a)–(d) correspond to $\rho_T f = 0.702$, 0.740, 0.772 and 0.790, respectively. The inset shows the same data in a log-linear representation. (b) Average dimer bond lifetime, τ, as a function of $\rho_T f$.

a log-linear representation. It shows a linear decay of the density functions, pointing out their exponential behaviour. Thus, for all cases, a good fit of an exponential density function can be achieved, pdf $= \exp(-t/\tau)/\tau$ (not shown), except for very short times (a number of steps below 25). Note that this definition of τ coincides with the one given in Section 2.2, i.e. the average dimer bond lifetime, since the average value of this pdf is τ.

For increasing $\rho_T f$, the pdf decreases for short times (few steps) and increases for large times. In other words, τ increases suggesting that there exists an attractive mean force A–A pair potential well, which deepens for larger $\rho_T f$ values. As mentioned elsewhere, this suggestion is in fact a well-known effect [36,37], which may lead to phase separation phenomena (for instance, this work) and assembling processes [38]. As the contact density at the surface of the dimer increases (not shown), the pressure which hinders the dimer breakup increases, producing larger τ values. In our case, the mean force A–A pair potential coincides with the contact (or depletion) contribution, since only an entropic term appears in the free energy expression of the system (there is no energetic term). In consequence, as the mean force A–A pair potential well deepens, more steps are needed in order to break the dimer, as easily seen in Figure 8(b) where τ is plotted against $\rho_T f$. The dashed line corresponds to the fit $\log \tau = 13.03 - 33.46(\rho_T f) + 25.17(\rho_T f)^2$. Again, extrapolation of the fit may lead to deviations.

3.6 e_{ij} matrix elements

As mentioned in Section 2.2, e_{ij} establishes the number of bonds inside an $(i+j)$-size cluster, which, on breakup, leads to i- and j-size fragments. This matrix was determined by analysing different structures generated by three-dimensional (3D) simulations in previous work [25]. The obtained result was

$$e_{ij}^{3d}(1+\delta_{ij}) = p_1^{3d}\left(i^{p_2^{3d}} + j^{p_2^{3d}}\right)\left(i^{-p_3^{3d}} + j^{-p_3^{3d}}\right)(ij)^{p_4^{3d}},$$

with $p_1^{3d} = 0.4391$, $p_2^{3d} = 1.006$, $p_3^{3d} = -1.007$ and $p_4^{3d} = -0.1363$, where super-index 3d stands for 3D reversible aggregation. In this work, we adopted the following expression:

$$e_{ij}(1+\delta_{ij}) = \frac{1}{2}\left(i^{p_1} + j^{p_1}\right)\left(i^{-p_1} + j^{-p_1}\right)(ij)^{p_2}, \quad (6)$$

with p_1 and p_2 being unknown parameters which depend on the structure of the formed clusters. Expression (6) has the advantage of having two fewer parameters than the 3d case. Here, the prefactor is forced to be 1/2 to make

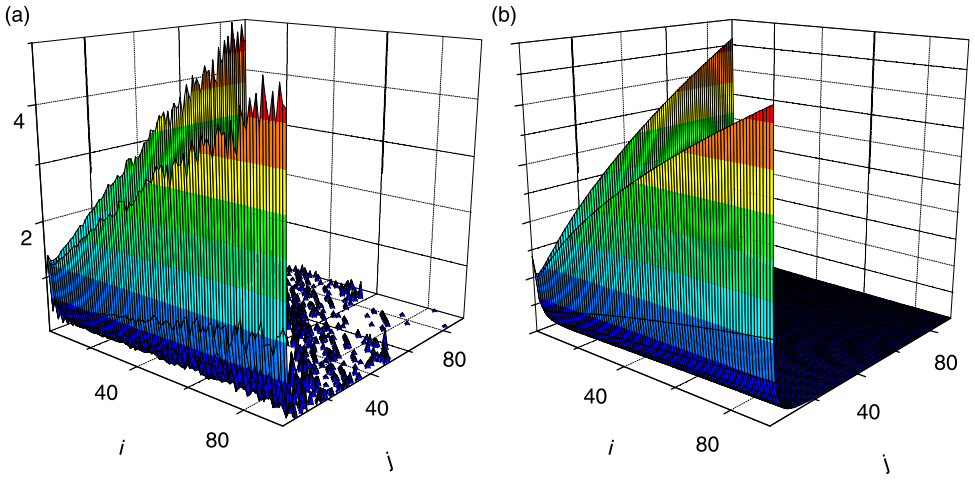

Figure 9. (a) e_{ij} as obtained from direct counting on the generated clusters for $X_A = 0.100$ and $\rho_T = 0.695$. (b) The corresponding $e_{ij}(1 + \delta_{ij})$ fit by using Expression (6).

$e_{11} = 1$. In addition, there are theoretical arguments to force the exponents of the second term to be the negative of those of the first term [39]. Indeed, for the 3d case, we obtained $p_2^{3d} = 1.006$ and $p_3^{3d} = -1.007$, which clearly support this statement.

It has also been noted, as stated by Babu et al. [39], that the use of Expressions (2), (3) and (6) for solving Equation (1) does not generally lead to a detailed balance condition. This condition represents a strong restriction of Equation (1) [16,40], which has been used to deal with reversible aggregation at equilibrium [41,42] since it leads to a simplification of the general mathematical expressions. Our choice is to deal with Equation (1) without imposing any restriction.

The direct counting on the generated clusters for $X_A = 0.100$ and $\rho_T = 0.695$ yields the data shown in Figure 9(a). By fitting Expression (6), we obtained $p_1 = 1.186$ and $p_2 = -0.741$, for this particular case [see the fit in Figure 9(b)]. It is easily observed that the small–large fragmentation is much more probable than the large–large breakup (shattering fragmentation). Indeed, the value of p_2 is much smaller than that of p_4^{3d}, indicating a lower large–large breakup frequency for the 2D case. This confirms that the large–large breakup is almost completely forbidden, as a consequence of the drop-like aggregate structure.

Since the structures compact for increasing $\rho_T f$ by producing a larger number of neighbours and loops, e_{ij} should also depend on $\rho_T f$ (loops and multiple bonds hinder breakup which is accounted by e_{ij}). Accordingly, parameters p_1 and p_2 must be calculated for each condition. By doing so, one obtains the data shown in Figure 10. Here, p_1 and p_2 are given as a function of $\rho_T f$. These parameters can be reasonably approached by $p_1 = 1.824 - 4.237(\rho_T f) + 4.454(\rho_T f)^2$ and $p_2 = -5.805 + 18.00(\rho_T f) - 15.01(\rho_T f)^2$. Therefore, the number of bonds inside a given large $(i + j)$-size cluster, which on breakup leads to i- and j-size fragments, decreases as $\rho_T f$ increases (p_2 decreases). Since, in turn, p_1 augments with $\rho_T f$, the e_{ij} decrease is not very pronounced for small i or j and very important for $i \simeq j$. In brief, the breakup of many internal bonds does not produce the cluster fragmentation since there is a large cluster interconnection. Consequently, the shattering regime enhances and the CSD splits into a population of very large and very small clusters for large $\rho_T f$ (phase separation).

3.7 *Stochastic solutions*

At this point we know the dependence of each parameter on $\rho_T f$, except for the proportional dimensionless constant C (which should be a constant for all cases), the average number of collisions the monomers perform when they are space-correlated, $\mathcal{N}_{11}$, and parameter b. Next, we tune these three free parameters (restricting C as a constant) to obtain solutions of Equation (1) to fit the data obtained by BD simulations. Details on the algorithm employed for solving Equation (1) are given elsewhere [25]. Since the initial configuration of simulations has some dimers and few trimers, we set a similar number of these oligomers in the initial conditions for solving Equation (1) ($<10\%$ in mass). The best overall fit leads to $C = 20$, and $\mathcal{N}_{11}$ and b as shown in Figure 11. The obtained stochastic solutions are compared to the simulations in Figure 12 for all studied conditions.

For all cases, the theoretical predictions and simulations shown in Figure 12 agree well. The first two columns of the figure show the evolution of the CSD where no phase separation occurs, whereas for columns three and four, the system phase separates. So, in the first group, the solid symbols (showing the equilibrium data) coincide with the long-time CSD obtained by the BD simulations. Additionally, in these cases, the cluster size distributes with a relatively large proportion of oligomers and no super-cluster (a drop having more than 81 A-particles) is seen. On the other hand, the second group

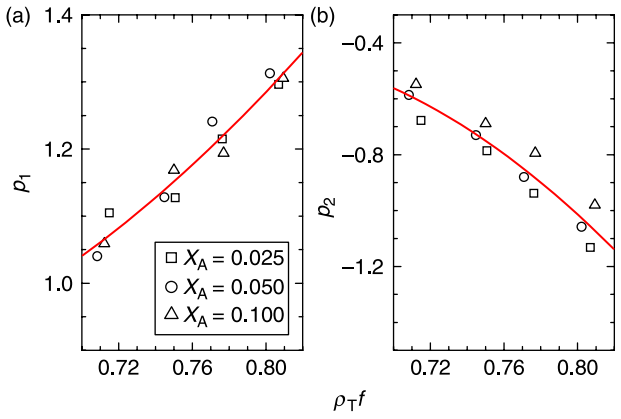

Figure 10. Parameters p_1 (a) and p_2 (b) as a function of $\rho_T f$.

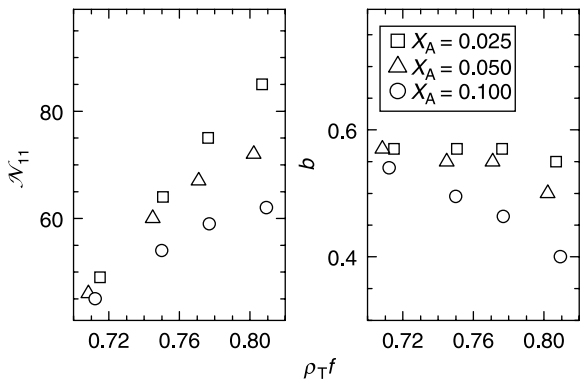

Figure 11. Fitted parameters $\mathcal{N}_{11}$ and b as a function of $\rho_T f$ for all conditions.

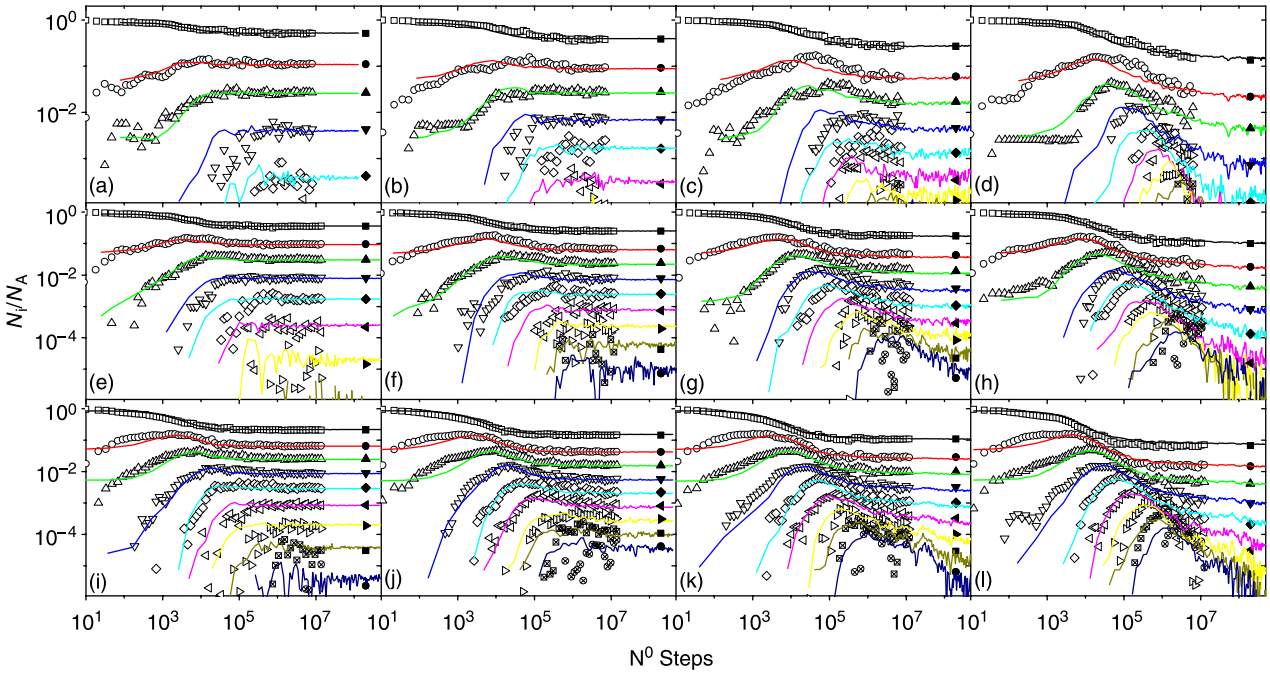

Figure 12. Evolution of the normalised CSD for all conditions. The labels on the graphs correspond to the conditions shown in Table 1. The symbols represent monomers up to 80-mers grouped in logarithmically spaced intervals; (□) monomers, (○) dimers, (△) 3–4-mers, (▽) 5–7-mers, (◇) 8– 12-mers, (◁) 13–20-mers, (▷) 21–32-mers, (⊠) 33–50-mers and (⊗) 51–80-mers. Solid symbols correspond to equilibrium. Lines are the stochastic solutions of the master equation.

is characterised by a larger time evolution for approaching equilibrium, which consists of the formation of a super-cluster (largest drop) and a depletion of the oligomer population. This larger time evolution is evidenced by the fact that solid symbols do not coincide with the long-time CSD obtained by the BD simulations. Nevertheless, in all cases, the stochastic solutions reach equilibrium in $< 10^9$ steps, and practically agree with the MC equilibrium data. Consequently, the stochastic approach also points out phase separation by producing a super-aggregate and a final CSD with a relative lack of oligomers.

The stochastic method also predicts two different mechanisms for the growing of the largest drop (not shown). The first mechanism is by coalescence with other smaller ones (aggregation). The second mechanism is produced by the diffusion of the monomer gas phase in quasi-equilibrium with the smallest drops towards the larger one, leading to an overall mass transference. This process is similar to the Ostwald ripening effect observed in micelles [43]. It should be noted that the time scale of both mechanisms is much larger than that accessed by the simulations, and so, the stochastic approach is useful to gain further insight into these long-time effects. These two mechanisms were already pointed out in previous work [40]. As mentioned in Section 3.6, e_{ij} is large for small i or j ($i + j$ = constant) and very small for similar i and j. This enhances the second mechanism, which in turn becomes relatively more important as the drops grow and their diffusion coefficients diminish.

The $\mathcal{N}_{11}$ values shown in Figure 11 are much larger than those reported in previous works [31,33,40], and it makes evident the very large values here reported. In this regard, there are three points to be noted. The first is that our simulations are 2D, instead of 3D. The second point is that we are working with a very crowded system, by explicitly accounting for the more concentrated species, B. Thus, the diffusion away of two A space-correlated particles is much more hindered. Finally, it should be noted that the value of $\mathcal{N}_{11}$ implicitly depends on the definition of the bonding radius, $r_b = 1.5\sigma$, employed for obtaining τ. By increasing r_b, the choice of which is somewhat arbitrary, τ increases and, as a consequence, the obtained fit of $\mathcal{N}_{11}$ decreases to keep a similar fragmentation kernel [see Expression (3)].

Figure 11 also shows the practically linear increase of $\mathcal{N}_{11}$ with $\rho_T f$ for $X_A = 0.025$. Although τ accounts for the increasing depth of the A–A pair potential well, it does not take into account the potential tail for A–A distances larger than r_b. Consequently, parameter $\mathcal{N}_{11}$ increases for compensating this fact (the effective fragmentation diminishes). On the other hand, parameter b keeps nearly constant around 0.55. This indicates that e_{ij} elements are independent of $\rho_T f$, as expected. Notwithstanding, for $X_A = 0.050$ and 0.100, there appear deviations from a

linear behaviour of $\mathcal{N}_{11}$ with $\rho_T f$, and from $b =$ constant at large $\rho_T f$. Indeed, for $X_A = 0.100$, deviations turn important even for intermediate values of $\rho_T f$. Our belief is that these deviations point out a dependence of τ with time, as a consequence of the system rearrangement, which our model does not account for. That is, the system evolves releasing free accessible space, shallowing the A–A pair potential well and, in turn, decreasing τ. This unconsidered effect is larger for A-concentrated systems, which affects the fitted parameters. Finally, one should keep in mind that the theoretical framework is expected to work for diluted conditions only.

From our point of view, one major goal of this work is the employment of a kinetic framework (the master equation and the aggregation and fragmentation kernels) to reproduce the binary mixture phase behaviour and separation kinetics. It should be noted that this framework contracts the vast statistical information of the system in just the CSD of the A-species, explicitly letting aside all particle positions and momenta. Therefore, it seems *a priori* difficult to describe the general behaviour of the system with this little piece of information. In fact, for achieving this goal, we had to introduce some matrices containing averages of some relevant structural information, such that defined by the e_{ij} elements, and some others accounting for some spatial cluster–cluster correlations, $\mathcal{N}_{ij}$. Without such averages (or others following the same spirit), the framework would not succeed. Hence, we would like to remark on the very nice agreement between the stochastic solutions and simulations depicted in Figure 12.

4. Conclusions

This work deals with the phase behaviour and kinetics of phase separation of a NAHD symmetric binary mixture in two dimensions. We reported the phase separation coexistence curve by means of a MC semigrand technique for the case of a non-additive parameter of $\Delta = 0.2$. In addition, BD simulations for conditions defined below and above the coexistence curve were performed to follow the less concentrated species aggregation kinetics. We found that clusters grow producing a stable distribution of oligomers for conditions below the coexistence curve, whereas the system evolves towards a polarised CSD having a rare cloud of very small clusters and a huge drop-like cluster for conditions above the coexistence curve.

Most of this paper, however, focuses on modelling the above depicted phenomenon with the use of a kinetic approach. To our knowledge, it is the first time this approach is employed to deal with a liquid–liquid phase separation phenomena. The approach provides a reduced description of the phase separation processes, and forces us to gain further insight, since relevant structural and dynamic information is needed in order to build the framework. Thus, the cluster fractal dimension, the monomer diffusion coefficient, the bonding cluster structure, the average dimer bond lifetime and the average number of collisions which two space-correlated clusters perform before diffusing away are measured as a function of the different system conditions. The framework, which employs this information and keeps a minimum of free physically based parameters (to guaranty a good level of confidence of the obtained results), turns out the evolution of the CSD to be compared to simulations. The good agreement obtained between theory and simulations and the correct behaviour of the fitted parameters signal the solid base and the consistency of the developed model.

Finally, we should emphasise that kinetics, basically characterised by diffusion coefficients and average bond times, gives rise to the same final states than equilibrium, which is mostly ruled by effective pair potential energies. This reveals a clear link between the two approaches, and evidences that the studied system does not present metastable regions.

Acknowledgements

This work is dedicated to the memory of our colleague and friend Yurko Duda. L.M.S. acknowledges the scholarship granted by the IMP and the CONACyT, through numbers 3588 and 85014, respectively.

References

[1] M.P. Allen and D.J. Tildesley, *Computer Simulation of Liquids*, Clarendon, Oxford, 1986.
[2] A.A. Louis, *Effective potentials for polymers and colloids: Beyond the van der Waals picture of fluids?*, Philos. Trans. Roy. Soc. A 359 (2001), pp. 939–960.
[3] A.A. Louis, E. Allahyarov, H. Löwen, and R. Roth, *Effective forces in colloidal mixtures: From depletion attraction to accumulation repulsion*, Phys. Rev. E 65 (2002), 061407.
[4] R.H. Perry and D.W. Green, *Perry's Chemical Engineers Handbook*, 6th ed., McGraw-Hill, New York, 1984.
[5] R. Tenne and E. Bergmann, *Scaled particle theory for mixtures of nonadditive hard discs*, J. Chem. Phys. 70 (1978), pp. 1952–1961.
[6] F. Saija and P.V. Giaquinta, *Monte Carlo simulation and phase behavior of nonadditive hard-core mixtures in two dimensions*, J. Chem. Phys. 117 (2002), pp. 5780–5784.
[7] Y. Duda and F. Vázquez, *Modeling of composite latex particle morphology by off-lattice Monte Carlo simulation*, Langmuir 21 (2005), pp. 1096–1102.
[8] M. Bárcenas, P. Orea, E. Buenrostro-González, L. Zamudio-Rivera, and Y. Duda, *Study of medium effect on asphaltene agglomeration inhibitor efficiency*, Energy Fuels 23 (2008), pp. 1917–1922.
[9] D. Frenkel, *The simulation of entropic phase transitions*, J. Phys.: Condens. Matter 6 (1994), pp. A71–A78.
[10] E.G. Batalin-Vikovisky, *Algebras and two dimensional topological field theories*, Commun. Math. Phys. 159 (1994), pp. 265–285.
[11] M. Thorn and M. Seesselberg, *Dynamic scaling in colloidal aggregation – comparison of experimental data with results of a stochastic simulation*, Phys. Rev. Lett. 72 (1994), pp. 3622–3625.
[12] M. Thorn, M.L. Broide, and M. Seesselberg, *Fluctuations in discrete fragmentation processes studied by stochastic simulations*, Phys. Rev. E 51 (1995), pp. 4089–4094.

[13] D.T. Gillespie, *Exact stochastic simulation of coupled chemical reactions*, J. Phys. Chem. 81 (1977), pp. 2340–2361.
[14] D.T. Gillespie, *The chemical Langevin equation*, J. Chem. Phys. 113 (2000), pp. 297–306.
[15] E. de Miguel, E.M. del Rio, and M. Telo da Gama, *Liquid–liquid phase equilibria of symmetrical mixtures by simulation in the semigrand canonical ensemble*, J. Chem. Phys. 103 (1995), pp. 6188–6196.
[16] D. Frenkel and B. Smit, *Understanding Molecular Simulation*, 2nd ed., Academic Press, New York, 2002.
[17] A. Buhot, *Cluster algorithm for nonadditive hard-core mixtures*, J. Chem. Phys. 122 (2005), 024105.
[18] K. Binder, *Critical properties from Monte-Carlo coarse graining and renormalization*, Phys. Rev. Lett. 47 (1982), pp. 693–696.
[19] H.P. Deutsch and K. Binder, *Critical-behavior and crossover scaling in symmetrical polymer mixtures – A Monte-Carlo investigation*, Macromolecules 25 (1992), pp. 6214–6230.
[20] K. Jagannathan and A. Yethiraj, *Monte Carlo simulations for the phase behavior of symmetric nonadditive hard sphere mixtures*, J. Chem. Phys. 118 (2003), pp. 7907–7911.
[21] K. Kikuchi, M. Yoshida, T. Maekawa, and H. Watanabe, *Metropolis Monte Carlo method as a numerical technique to solve the Fokker-Plank equation*, Chem. Phys. Lett. 185 (1991), pp. 335–338.
[22] D.M. Heyes and A.C. Brańka, *Monte Carlo as Brownian Dynamics*, Mol. Phys. 94 (1998), pp. 447–454.
[23] M. von Smoluchowski, *Drei Vorträge über Diffusion, Brownsche Molekularbewegung und Koagulation von Kolloidteilchen*, Phys. Z. 17 (1916), pp. 557–571.
[24] M. von Smoluchowski, *Versuch einer mathematischen Theorie der Koagulationskinetik kolloider Lösungen*, Phys. Z. Chem. 92 (1917), pp. 129–168.
[25] G. Odriozola, A. Schmitt, A. Moncho-Jordá, J. Callejas-Fernández, R. Martínez-García, R. Leone, and R. Hidalgo-Álvarez, *Constant bond breakup probability model for reversible aggregation processes*, Phys. Rev. E 65 (2002), 031405.
[26] R. Jullien, *The application of fractals to colloidal aggregation*, Croat. Chem. Acta 65 (1992), pp. 215–235.
[27] P. Meakin, *Simulation of the kinetics of aggregation: Fractals and scaling*, Croat. Chem. Acta 65 (1992), pp. 237–267.
[28] A. Moncho-Jordá, G. Odriozola, F. Martínez-López, A. Schmitt, and R. Hidalgo-Álvarez, *The DLCA-RLCA transition arising in 2D aggregation: Simulations and mean field theory*, Eur. Phys. J. E 5 (2001), pp. 471–480.
[29] M.Y. Lin, H.M. Lindsay, D.A. Weitz, R.C. Ball, R. Klein, and P. Meakin, *Universality in colloid aggregation*, Nature (London) 339 (1989), pp. 360–362.
[30] M.Y. Lin, H.M. Lindsay, D.A. Weitz, R. Klein, R.C. Ball, and P. Meakin, *Universal diffusion-limited colloid aggregation*, Phys. Condens. Matter 2 (1990), pp. 3093–3113.
[31] G. Odriozola, A. Moncho-Jordá, A. Schmitt, J. Callejas-Fernández, R. Martínez-García, and R. Hidalgo-Álvarez, *A probabilistic aggregation kernel for the computer-simulated transition from DLCA to RLCA*, Europhys. Lett. 53 (2001), pp. 797–803.
[32] M. Lattuada, P. Sandkuhler, H. Wu, J. Sefcik, and M. Morbidelli, *Aggregation kinetics of polymer colloids in reaction limited regime: Experiments and simulations*, Adv. Colloid Interface Sci. 103 (2003), pp. 33–56.
[33] M. Lattuada, H. Wu, J. Sefcik, and M. Morbidelli, *Detailed model of the aggregation event between two fractal clusters*, J. Phys. Chem. B 110 (2006), pp. 6574–6586.
[34] L.V. Woodcock and C.A. Angell, *Diffusivity of the hard-sphere model in the region of fluid metastability*, Phys. Rev. Lett. 47 (1981), pp. 1129–1132.
[35] D.J. Robinson and J.C. Earnshaw, *Experimental-study of colloidal aggregation in 2 dimensions.1. Structural aspects*, Phys. Rev. A 46 (1992), pp. 2045–2054.
[36] Y. Duda, *Interaction between colloids in network forming solution*, J. Colloid Interface Sci. 208 (1999), pp. 279–286.
[37] Y. Duda, *Stability of colloids in chemically reacting network-forming solvent*, J. Colloid Interface Sci. 213 (1999), pp. 498–505.
[38] G. Odriozola, F. Jiménez-Ángeles, and M. Lozada-Cassou, *Entropy driven key-lock assembly*, J. Chem. Phys. 129 (2008), 111101.
[39] S. Babu, M. Rottereau, T. Nicolai, J.C. Gimel, and D. Durand, *Flocculation and percolation in reversible cluster-cluster aggregation*, Eur. Phys. J. E 19 (2006), pp. 203–211.
[40] A.M. Puertas and G. Odriozola, *Linking phase behavior and reversible colloidal aggregation at low concentrations: Simulations and stochastic mean field theory*, J. Phys. Chem. B 111 (2007), pp. 5564–5572.
[41] S. Babu, J.C. Gimel, and T. Nicolai, *Phase separation and percolation of reversibly aggregating spheres with a square-well attraction potential*, J. Chem. Phys. 125 (2006), 184512.
[42] F. Family, P. Meakin, and J.M. Deutch, *Kinetics of coagulation with fragmentation – scaling behavior and fluctuations*, Phys. Rev. Lett. 57 (1986), pp. 727–730.
[43] W. Ostwald, *Lehrbuch der Allgemeinen Chemie*, 2nd ed., Verlag von Wilheim Engelmann, Leipzig, 1896.